

Impact of Interlayer Application on Band Bending for Improved Electron Extraction for Efficient Flexible Perovskite Mini-Modules

*Stefano Pisoni¹, Fan Fu^{1†}, Roland Widmer², Romain Carron¹, Thierry Moser¹, Oliver Groening²,
Ayodhya N. Tiwari¹ and Stephan Buecheler¹*

¹Laboratory for Thin Films and Photovoltaics, Empa-Swiss Federal Laboratories for Materials Science and Technology, Ueberlandstrasse 129, 8600 Duebendorf, Switzerland.

²Nanotech@surfaces Laboratory, Empa-Swiss Federal Laboratories for Materials Science and Technology, Ueberlandstrasse 129, 8600 Duebendorf, Switzerland.

[†]now at Photovoltaics and Thin-Film Electronics Laboratory (PV-Lab), Ecole Polytechnique Fédérale de Lausanne (EPFL), Rue de la Maladière 71b, 2002 Neuchâtel, Switzerland.

KEYWORDS: perovskite solar cell, flexible, solar module, interlayer, laser scribing

This document is the accepted manuscript version of the following article:
Pisoni, S., Fu, F., Widmer, R., Carron, R., Moser, T., Groening, O., ... Buecheler, S.
(2018). Impact of interlayer application on band bending for improved electron
extraction for efficient flexible perovskite mini-modules. *Nano Energy*, 49, 300-307.
<http://doi.org/10.1016/j.nanoen.2018.04.056>

This manuscript version is made available under the CC-BY-NC-ND 4.0 license <http://creativecommons.org/licenses/by-nc-nd/4.0/>

ABSTRACT:

The development of highly efficient lightweight flexible perovskite solar cells (PSCs) opens the way to high-throughput roll-to-roll manufacturing processes and new applications such as building integration and mobile products. Flexible PSCs are generally realized on small areas ($<0.2 \text{ cm}^2$), far from technology commercialization where modules-scale is necessary. In this work, we demonstrate highly efficient *n-i-p* PSCs grown on flexible substrates by proper interface engineering for improved electron extraction. We compared spin coated PEIE and vacuum deposited LiF as interlayers between Al-doped ZnO, as transport conductive oxide (TCO), and thermally evaporated C_{60} , as electron transport layer (ETL). Once interlayers are applied, we observed a favorable band bending at TCO interface which results in enhanced charge extraction and lower recombination losses. We achieved flexible PSCs with stabilized efficiencies of 14.8%, both with PEIE and LiF interfacial modifications.

In addition, we developed a flexible perovskite mini-module with stabilized efficiency of 10.5% onto an aperture area larger than 10 cm^2 . The monolithic interconnections are entirely obtained by highly accurate and reliable laser scribing methods. A geometric fill factor as high as $\sim 94\%$ is achieved, with a dead area width of $\sim 250 \text{ }\mu\text{m}$.

1. Introduction

In the past few years, perovskite solar cells (PSCs) have achieved impressive efficiencies (above 22%) [1] thanks to their high absorption coefficient, long charge-carrier diffusion length and defect tolerance [2, 3]. In addition, PSCs can be developed on flexible substrates paving the way to high-throughput roll-to-roll manufacturing, lightweight mobile applications and advanced building-integration. Low-temperature processing is necessary to realize PSCs on flexible plastic substrate, which forbids the use of mesoporous TiO_2 scaffold ($>450^\circ\text{C}$ sintering step) as highly efficient electron transport layer (ETL) [1, 4]. For these reasons, many efforts have been focused on developing efficient ETLs via low-temperature deposition [5, 6].

Commonly, flexible PSCs are developed on indium tin oxide (ITO)-coated plastic substrates [7].

However, there is still a lack of understanding and investigation of charge extraction at the interface between low-temperature ETLs and alternative transparent conductive oxides (TCOs).

Al-doped ZnO (AZO) is a promising alternative to ITO for its low cost, composition based on earth-abundant elements and for its high near-infrared transmittance which opens the way to new flexible thin-film tandem concepts [8]. So far, only moderate device efficiency ($\sim 7\%$) has been obtained for flexible PSCs based on AZO [9]. Improvements in performances (13.2%) were achieved using undoped ZnO as ETL [8], which, however, poses a source of instability for $\text{CH}_3\text{NH}_3\text{PbI}_3$ (MAPI) under moderate annealing temperatures ($\sim 100^\circ\text{C}$) due to deprotonation of the CH_3NH_3^+ cation [10]. Therefore, low-temperature deposited ETLs and ETL/AZO interfaces need to be developed and engineered to have reduced energy barriers for electrons extraction and low interface recombination losses.

In order to get one step closer to industrial implementation, upscaling from individual solar cells to module sizes is required.

A thin-film solar module is fabricated by serial interconnection of solar cells, which is mainly based on three patterning steps, two scribes (P1 and P3) are necessary for electrical separation of the front and rear contacts between cells, while one scribe (P2) is needed to create an electrical interconnection between the anode and the cathode of adjacent cells [11]. The area between P1 and P3 does not contribute to the photocurrent (dead area); hence, it is necessary to keep the scribing lines and their separations as narrow as possible.

Only few works on flexible perovskite mini-modules have been reported up to now. Di Giacomo et al. developed a flexible perovskite mini-module on ITO/PET substrate, with an efficiency of 3.1% onto an active area of 7.9 cm^2 with scribing procedures based on masking, laser definition and self-patterning [12]. Yeo et al. demonstrated a flexible perovskite mini-module with 8.1% efficiency onto an active area of 10 cm^2 (P1 obtained by wet-etching of ITO substrate, P2 by mechanical scribing and P3 by use of shadow masks) [13]. These scribing methods for serial interconnections are not suitable for high speed and large-area industrial manufacturing.

Therefore, more reliable, high speed and scalable patterning methods should be considered in order to minimize dead area losses improving mini-module performances. Recently, Dagar et al. reported fully laser-scribed flexible perovskite mini-module onto an active area of 12 cm^2 with an efficiency of 5.7% and 8.8% when measured in forward and backward direction, respectively [14]. Limited charge transport and detrimental pile-up at ETL interface could result in hysteresis and poor efficiencies [15].

These mini-module performances (not steady-state values and with significant hysteresis) still lag far behind the performances of small flexible PSCs ($< 0.2 \text{ cm}^2$ with efficiencies $> 14\%$) [14]. Here we report flexible PSCs with sputtered AZO as TCO and thermally evaporated C_{60} as ETL. Limited charge transport due to an unfavorable band bending at ETL/TCO interface is observed,

which constrains device performances. We show that interfacial modification by spin coated poly(ethylenimine) ethoxilated (PEIE) or thermally evaporated lithium fluoride (LiF) gives rise to favorable band bending and enhanced charge extraction at the interface with TCO.

Particularly, LiF interfacial modification induces a stronger modulation of electrostatic potential with a more severe downward band bending at ETL/TCO interface compared to PEIE one.

Flexible PSCs with steady-state efficiency of 14.8% are demonstrated, using LiF as interlayer between AZO and C₆₀ in a traditional *n-i-p* structure.

In addition, the use of vacuum deposited interlayer and ETL opens the opportunity to mini-module up-scaling. We demonstrate monolithically-integrated flexible perovskite mini-module with a steady-state efficiency of 10.5% onto an aperture area of 10.2 cm², relying only on laser scribing as patterning method for P1, P2 and P3 interconnections. A geometric fill factor (GFF) of ~94% is achieved.

2. Results and discussion

We have developed PSCs on a flexible substrate which is commonly used as front encapsulation foil for flexible Cu(InGa)Se₂ (CIGS) solar modules. This substrate exhibits a higher transmittance and orders of magnitude lower water-vapor transmission rate (WVTR) values with respect to commonly used uncoated PET and PEN flexible substrates. As we already reported [8], highly near infrared (NIR)-transparent AZO is used as TCO.

Thermally evaporated C₆₀ is used as ETL to suppress *J-V* hysteresis and to ensure compact growth of perovskite absorber [8].

Fig.1 displays the photovoltaic performances of the flexible PSC. The *J-V* characteristics show an open-circuit voltage (V_{oc}) of 1.03 V, a short-circuit current (J_{sc}) of 18.0 mA cm⁻², and a fill

factor (FF) of 65.0 % measured in the forward direction, while a V_{oc} of 1.01 V, a J_{sc} of 17.7 mA cm⁻², a FF of 69.9 % when measured in the backward direction (Fig. 1a). Fig. 1b presents the photovoltaic parameters at maximum power point (MPP) as a function of time. The device shows steady-state efficiency (η_{MPP}) of 12.8% with J_{MPP} of 15.5 mA cm⁻² and V_{MPP} of 0.82 V.

The integrated short-circuit current density obtained from the external quantum efficiency (EQE) spectrum (18.2 mA cm⁻²) agrees with that obtained from J - V curves. This indicates that, for our PSCs, any spectral mismatch between the simulator and AM1.5G standard solar radiation is negligible (Fig. 1c). The cross-section SEM image (Fig. 1d) confirms a compact absorber layer obtained by two-step vacuum/solution deposition. Fig. S1 shows a histogram of efficiencies obtained from 14 flexible perovskite solar cells with C₆₀ as ETL.

Although the flexible PSC displays decent efficiencies there is still room for improvement. Using ultraviolet photoelectron spectroscopy (UPS using He I 21.2 eV excitation), we show that the ETL/TCO interface is a limiting factor for device performances.

The UPS measurements show that the work function of AZO on flexible substrate is 3.83 (±0.05) eV. Once C₆₀ is thermally evaporated on AZO (ex-situ evaporation), the work function is reduced to 3.58 (±0.03) eV (Fig.2 a and b). This induces a slight, yet unfavorable upward band bending at C₆₀/AZO interface, hence a barrier against efficient extraction and collection of photogenerated electrons of about 0.2 eV (Fig. 2c).

ETL/TCO interfacial modification, which can modulate the electrostatic potential by dipoles formation, is a promising approach to enhance charge collection from the organic layer to the cathode (metal or TCO) [16].

Polyelectrolyte interfacial modifiers have been demonstrated to improve charge extraction and suppress trap-assisted recombination [17, 18]. As well, LiF interlayer has been proved beneficial in *p-i-n* PSCs when applied between ETL and metal back contact [19].

We have investigated two approaches to enhance charge collection at ETL/TCO interface by inducing favorable electrostatic potential modulation: spin coating of PEIE and thermal evaporation of LiF.

Fig. 3 displays the flexible PSC with PEIE interfacial modification. Fig. 3a and b show a schematic of the PEIE interface modification and the cross-section SEM image of the full device. The cell reaches a V_{oc} of 1.05 V, a J_{sc} of 18.6 mA cm⁻², and a FF of 75.7% measured in the forward direction, while a V_{oc} of 1.03 V, a J_{sc} of 18.2 mA cm⁻², a FF of 73.6% when measured in the backward direction (Fig. 3c). The device shows an η_{MPP} of 14.8% with J_{MPP} of 17.0 mA cm⁻² and V_{MPP} of 0.87 V (Fig. 3d). As shown in Fig. 3e, the J_{sc} value measured under solar simulator is comparable to the one obtained by integrating the absolute EQE over the AM1.5G spectrum (Fig. 3e). The statistics of 16 flexible devices with PEIE as interlayer is shown in Fig. S2.

The results prove that PEIE interfacial modification is beneficial, enhancing the efficiency by an absolute 2%.

We investigated vacuum deposited lithium fluoride (LiF) as possible alternative to spin coated PEIE interlayer in a “traditional” *n-i-p* PSC structure. Fig. 4 presents the flexible device with LiF interlayer. Fig. 4a and b shows a schematic of the interfacial layer modification and the cross-section SEM image of the full device stack. As presented in Fig. 4c, under forward measurement the cell displays a V_{oc} of 1.09 V, a J_{sc} of 18.3 mA cm⁻², and a FF of 70.4%, while, under backward measurement, a V_{oc} of 1.07 V, a J_{sc} of 18.2 mA cm⁻², and a FF of 74.4%. The device reaches an η_{MPP} of 14.8%, a J_{MPP} of 16.7 mA cm⁻² and a V_{MPP} of 0.89 V under continuous

illumination at MPP (Fig. 4d). The integrated short-circuit current density obtained from the external quantum efficiency (EQE) spectrum (18.3 mA cm^{-2}) matches well with that obtained from J - V curve (Fig. 4e). Fig. S3 presents the statistics of 14 flexible perovskite solar cells using thermally evaporated LiF as interlayer.

As for the PEIE case, we observed an absolute gain in efficiency of 2% with respect to the device without interfacial modification. Fig. S4a and b show a comparison of illuminated and corresponding dark J - V characteristics for the different devices with and without interlayers. Dark current-voltage measurements provide an effective way to determine fundamental performance parameters, such as ideality factor (n), saturation current density (J_0), series resistance (R_S) and shunt resistance (R_{SH}). Tab. S1 displays n , J_0 , R_S and R_{SH} values for the three different devices extracted from fit of data to a single diode model with two resistors. The parameter J_0 is the recombination current density in thermal equilibrium [20]. When an interlayer is applied, either PEIE or LiF, J_0 is decreased, indicating a reduction of recombination.

Although thin interlayers are deposited, their poor conductivity results in a slightly higher R_S with respect to devices without interfacial modification. When LiF is applied as interlayer R_{SH} is increased by one order of magnitude, which indicates reduction of possible alternative shunting paths for photo-generated carriers, similar to the effect of thin silicon oxide layers employed in thin-film silicon solar cell, as mentioned elsewhere [21, 22].

To get a deeper insight on how the interlayers can affect the electron extraction and collection, we carried out steady-state photoluminescence (PL). A stronger PL quenching is observed when PEIE or LiF interlayers are applied with respect to the stack without any interlayer (Fig. 5a). This indicates a more efficient and rapid electrons extraction across the interface.

To further prove the enhanced charge extraction and to assess energy levels shift at ETL/TCO interface, we show UPS measurements. Fig. 5b displays the UPS spectra of the valence states for AZO, C₆₀/AZO, PEIE/AZO, LiF/AZO, C₆₀/PEIE/AZO and C₆₀/LiF/AZO on flexible substrates. The energy position of the C₆₀ HOMO and HOMO-1 states at 2.32 eV and 3.65 eV, respectively, is largely independent of the interlayer structure and is consistent with values for multilayer films on metallic substrates [23]. This indicates that Fermi level alignment is reached in all three cases. Fig. 5c displays the UPS spectra of the secondary electron emission cut-off region of the same films as in Fig. 5b. As mentioned previously (Fig. 2), the work function of AZO on flexible substrate is 3.83 eV and, once C₆₀ is deposited on AZO, the work function is reduced to 3.58 eV, inducing an unfavorable upward band bending.

On the other hand, the work function of AZO surface coated with PEIE interlayer amounts to 3.33 (±0.05) eV (vacuum level down shift of about 0.4 eV). This will lead to a modulation of the electrostatic potential of the system once C₆₀ is deposited onto PEIE. In the present case of Fermi level alignment the electrostatic potential will induce a band bending across the interface. The specific profile of the electrostatic potential will depend on the charge distribution after charge transfer and on the dielectric constant of the materials. The work function of the system, when C₆₀ is deposited on PEIE/AZO, results to be equal to 3.54 (±0.01) eV. This leads to a favorable downward band bending (~0.2 eV) at the interface between C₆₀ and AZO, favoring electrons extraction and collection from the ETL to the TCO (Fig. 5d).

The same situation should apply for LiF interlayer. However, we observe a stronger vacuum level down shift when LiF is applied on AZO (new work function at 2.73 (±0.12) eV), which will induce a stronger modulation of the electrostatic potential of the system. A more pronounced

downward band bending (~ 0.8 eV) is present at the interface with C_{60} (the work function of C_{60} on LiF/AZO results to be $3.56 (\pm 0.02)$ eV) (Fig. 5e).

The favorable band bending improves electrons extraction from C_{60} and induces hole blocking properties at the interface, which supports the observations of enhancement in V_{oc} and FF of devices when interlayers are applied. In order to further improve the performances, deposition approaches for higher quality absorber are under investigation and will be described in a separate publication.

Upscaling of the device area is an important step towards commercialization of PSC technology. It is necessary to use deposition methods which are better suited for large area processing. For this reason, we selected vacuum deposited LiF, instead of spin coated PEIE, as interlayer between ETL and TCO.

To verify the scalability potential of our flexible device structure with thermally evaporated LiF interfacial modification, we realized flexible perovskite mini-modules with an aperture area of 10.2 cm^2 . We use laser scribing methods for monolithically interconnections, which are particularly suitable for soft and flexible plastic substrates [11]. While laser patterning has been successfully established for highly performing glass-based modules [24], its application has yet to be demonstrated to realize efficient flexible perovskite modules. The photograph of the flexible mini-module is shown in Fig. 6a. The 8 sub-cells, each one with a 1.2 cm^2 area, were serially interconnected by P1, P2 and P3 laser scribing as schematically shown in Fig. 6b. The details of the laser scribing procedure are presented in the experimental section.

The J - V characteristics show a V_{oc} of 7.5 V, a J_{sc} of 2.1 mA cm^{-2} , and a FF of 64.1 % measured in the forward direction, while a V_{oc} of 7.3 V, a J_{sc} of 2.1 mA cm^{-2} , a FF of 67.5 %, when measured in the backward direction (Fig. 6c). As presented in Fig. 6d, the device shows an η_{MPP}

of 10.5%, a J_{MPP} of 1.8 mA cm⁻² and a V_{MPP} of 5.9 V. Electroluminescence imaging confirms that all the 8 sub-cells are working (Fig. S5a). The above performances refer to the aperture area of the mini-module.

Fig. S5b displays a top-view SEM image of the three scribing steps, where the dead area width is as small as $\sim 250 \mu\text{m}$. Thanks to the precise laser scribing method, we are able to achieve a GFF of $\sim 94\%$ which is close to the current record achieved for perovskite mini-modules on glass [25].

3. Conclusions

We observed that the interface between AZO and C₆₀ represents a bottleneck for flexible PSC performances. As observed by UPS, an unfavorable band bending arises at the ETL/TCO interface. We successfully improved the power conversion efficiency of *n-i-p* PSCs by application of specific interlayers. With both solution-processed PEIE and vacuum deposited LiF interlayers we are able to achieve an absolute gain in efficiency of 2% with respect to the device without interlayers (from 12.8% to 14.8% stabilized efficiency). Further characterizations (PL and dark *J-V* curves) demonstrated a better charge extraction/collection, reduction of interfacial recombination losses and enhanced shunt blocking properties when interlayers are applied.

In addition, a modulation of electrostatic potential is observed (verified by UPS measurements) inducing a favorable downward band bending at the ETL/TCO interface, more pronounced in the case of LiF.

Focusing on the use of vacuum deposited LiF interlayer, better suited for large area processing, we demonstrated a flexible perovskite mini-module with a stabilized efficiency of 10.5% onto an aperture area greater than 10 cm².

All-laser scribing method was successfully used to develop the monolithically interconnected flexible mini-module with low dead area losses. This precise and accurate approach yields a GFF of ~94%, among the highest values reported so far.

4. Experimental section

4.1. Device Fabrication

PSCs are grown on flexible foil which is used as moisture barrier front sheet for encapsulation in flexible CIGS modules. 5 cm × 5 cm size flexible substrates are washed by hand followed by ultrasonic soap and water baths. The substrates are dried in vacuum for one week and cut into 4 quarters. Prior to further processing, 600 nm of compact ZnO:Al layer is deposited at room temperature by RF sputtering from a ceramic ZnO target (containing 2 at% Al₂O₃). The sheet resistance of as-deposited film on glass is around 20 Ω_□ measured by 4-probe method. Then, AZO layer was treated for 10 min under UV light for all the samples. For interfacial modification we compared two interlayers:

- 1) PEIE in deionized water (0.1% w/w) was deposited onto AZO layer by spin coating (5000 rpm, 5000 rpm s⁻¹ for 60 s) and subsequent annealing at 100°C for 10 minutes.
- 2) LiF (0.5 nm, equivalent thickness) was thermally evaporated in a N₂ filled glove-box on top of AZO at a rate 0.1-0.2 Å s⁻¹, at 5×10⁻⁴ Pa pressure.

Then, 7.5 nm of C60 is thermally evaporated in the N₂ filled glove-box on top of the TCO with or without interlayers. The PbI₂ film is thermally evaporated at a deposition pressure of 2-6 ×10⁻⁶ Pa. The deposition rate is controlled within 1.4-1.5 Å s⁻¹, monitored by a quartz crystal microbalance. The thickness of PbI₂ is 140 nm. After the PbI₂ deposition, the samples are subsequently transferred into a N₂ filled glove-box for further processing. The perovskite layer is

formed by spin coating of $\text{CH}_3\text{NH}_3\text{I}$ in 2-propanol at a concentration of 55 mg mL^{-1} . The solution is first spread to cover the whole substrate, and wait for 5 s before starting the rotation (4000 rpm , 4000 rpm s^{-1} for 40 s). The as-prepared films are annealed at 100°C for 30 minutes on a hotplate inside the glovebox. After annealing, the samples are cooled down to room temperature and $100 \mu\text{L}$ of a Spiro-OMeTAD solution (78.2 mg 2,2',7,7'-tetrakis-(N,N'-di-p-methoxyphenylamine)-9,9'-spirobifluorene (Spiro-OMeTAD), $33 \mu\text{L}$ lithium-bis(trifluoromethanesulfonyl)imide (Li-TFSI) solution (170 mg Li-TFSI in 1 mL acetonitrile, Sigma-Aldrich), and $8.2 \mu\text{L}$ 4-tertbutylpyridine (TBP) all dissolved in 1 mL of chlorobenzene (Sigma-Aldrich)) is spin coated on top of perovskite at 2500 rpm , 2500 rpm s^{-1} for 45 s. The devices are finished by evaporating 50 nm Au through a metal mask under high vacuum ($<3 \times 10^{-4} \text{ Pa}$). The solar cell area is equal to 0.15 cm^2 .

The monolithically integrated flexible perovskite mini-modules are developed with laser scribing methods. The following scribing parameters are used:

P1: wavelength= 1064 nm , ps laser

P2: wavelength= 1070 nm , quasi-CW laser

P3: wavelength= 1064 nm , ps laser

P1 is realized after the deposition of AZO, P2 after the deposition of Spiro-OMeTAD and P3 after the deposition of gold back contact.

4.2. Device characterization

The current density-voltage characteristics of PSCs are measured under standard simulated AM1.5G illumination using a Keithley 2400 source meter. The illumination intensity is calibrated to 1000 W m^{-2} using a certified single crystalline silicon solar cell. The $J-V$ measurement is performed in both forward (from -0.1 V to 1.4 V) and backward (from 1.4 V to -

0.1 V) direction separately without any pretreatment (e.g., light soaking, holding at forward bias for certain time etc.). The scan rate and delay time are 0.3 V s^{-1} and 10 ms, respectively. The external quantum efficiency is measured with a lock-in amplifier. The probing beam is generated by a chopped white source (900 W, halogen lamp, 260 Hz) and a grating monochromator. The beam size is adjusted to ensure that the illumination area is fully inside the cell area. A certified single crystalline silicon solar cell is used as the reference cell. White light bias is applied during the measurement with ~ 0.1 sun intensity. The steady-state efficiency as a function of time is recorded using a maximum power point tracker, which adjusts the applied voltage in order to reach the maximum power point (perturb and observe algorithm). The starting voltage is set to be 0.1 V.

X-ray diffraction patterns were obtained in Bragg-Brentano geometry by using a X'Pert PRO θ - 2θ scan (Cu- $K_{\alpha 1}$ radiation, $\lambda = 1.5406 \text{ \AA}$) from 10 to 60° (2θ) with a step interval of 0.0167° .

The SEM images of the samples were investigated with a Hitachi using 5 kV voltage and 10 mA. A thin layer of Pt (1 nm) was sputtered on top of the sample to avoid charging effect.

For photoluminescence (PL) measurements, the laser was set to continuous wave mode at about 77 W cm^{-2} . The spot has a diameter around $50 \text{ }\mu\text{m}$. The spectrally integrated luminescence decay was measured using a Picoquant PMA-C 192-M photomultiplier tube and a Picoquant TimeHarp 260 digitizing system with 50 ps time channel width.

UPS measurements were performed at room temperature (system base pressure below 1 e^{-10} mbar) using a HIS14 from Focus GmbH with He I ($h\nu = 21.2 \text{ eV}$) excitation at a pressure of 6 e^{-8} mbar and measured with a Scienta R3000 Analyzer. A cleaned Au(111) surface was used as a work function and Fermi edge reference for the UPS analysis.

Acknowledgements

Financial funding from Swiss National Science Foundation (SNF)-NRP70, PV2050 (project NO.: 407040_153976 and 407040_153916), SNF-NanoTera and Swiss Federal Office of Energy (SYNERGY: 20NA21_150950), NanoTera (project Synergy Gateway) and FP7 APPOLO project (609355). A special thank goes to Roger Ziltener for his contribution in mini-modules realization.

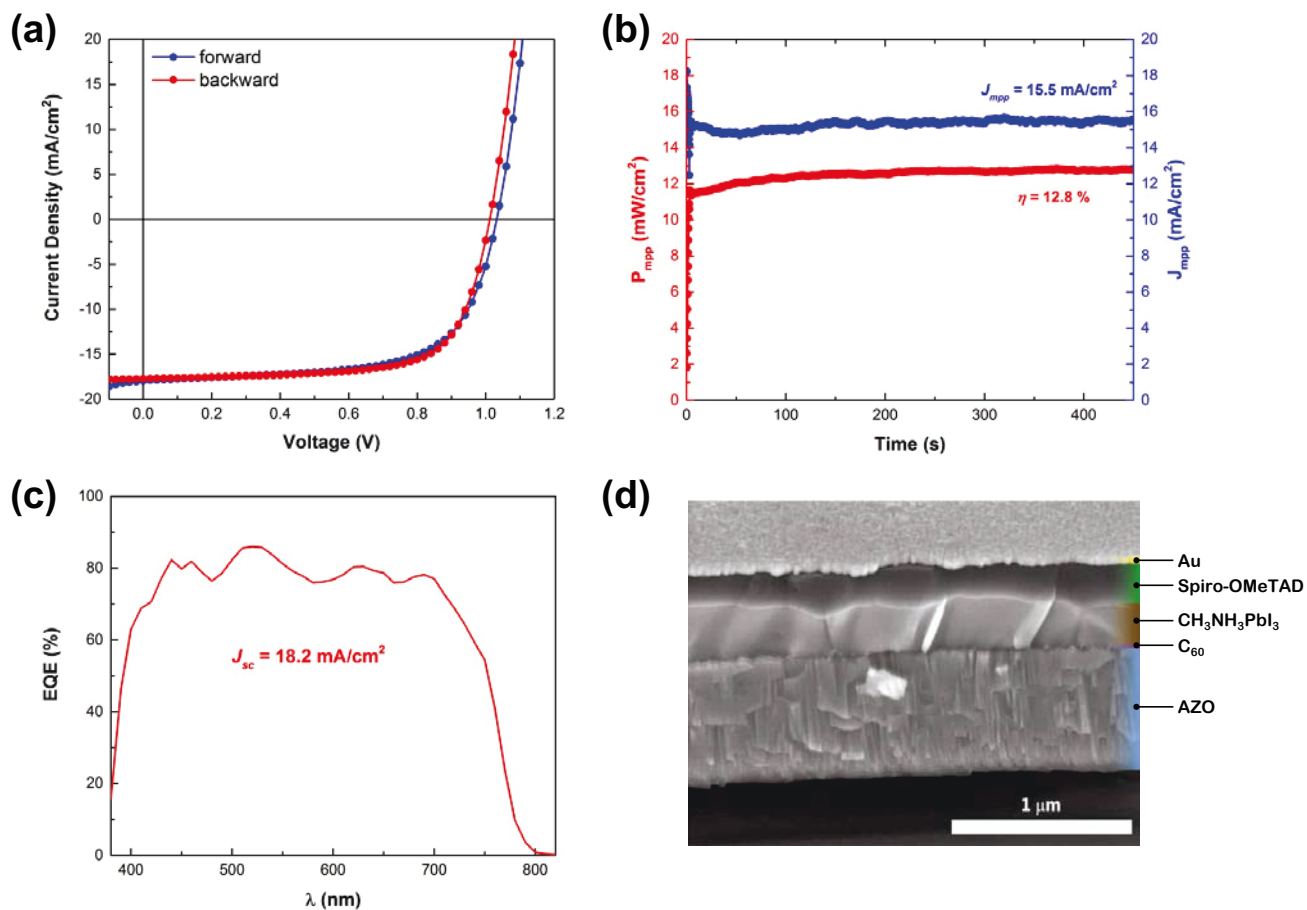


Fig. 1. (a) J - V curves in the forward (blue line), -0.1 V to 1.4 V, and the backward scan (red line), 1.4 V to -0.1 V, measured under standard test conditions. (b) Steady-state output at the MPP of the cell under continuous simulated AM1.5G one sun illumination. Stabilized power output (red line) and J_{MPP} (blue line). (c) External quantum efficiency (EQE) spectrum. The calculated J_{sc} from the EQE curve is 18.2 mA cm^{-2} . (d) Cross-section SEM image of the flexible PSC (scale bar $1 \mu\text{m}$).

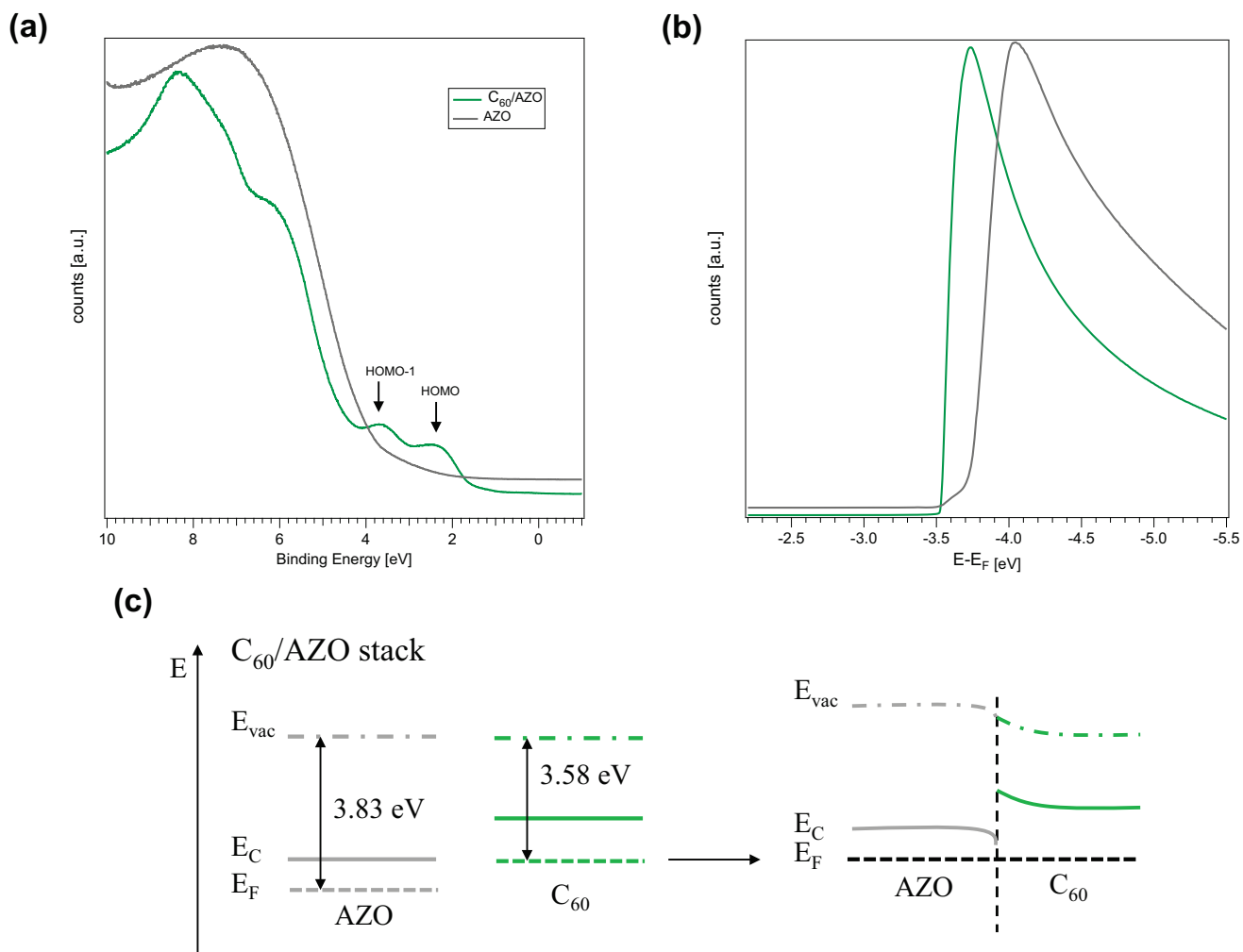


Fig. 2. (a) He I (21.2 eV) UPS spectra of the valence states for AZO and C₆₀/AZO flexible substrates. (b) Secondary electron cut-off region of the UPS spectra shown in (a) (the spectra are vertically offset for better visibility). (c) Schematics of electrostatic potential modulation once C₆₀ is deposited on AZO.

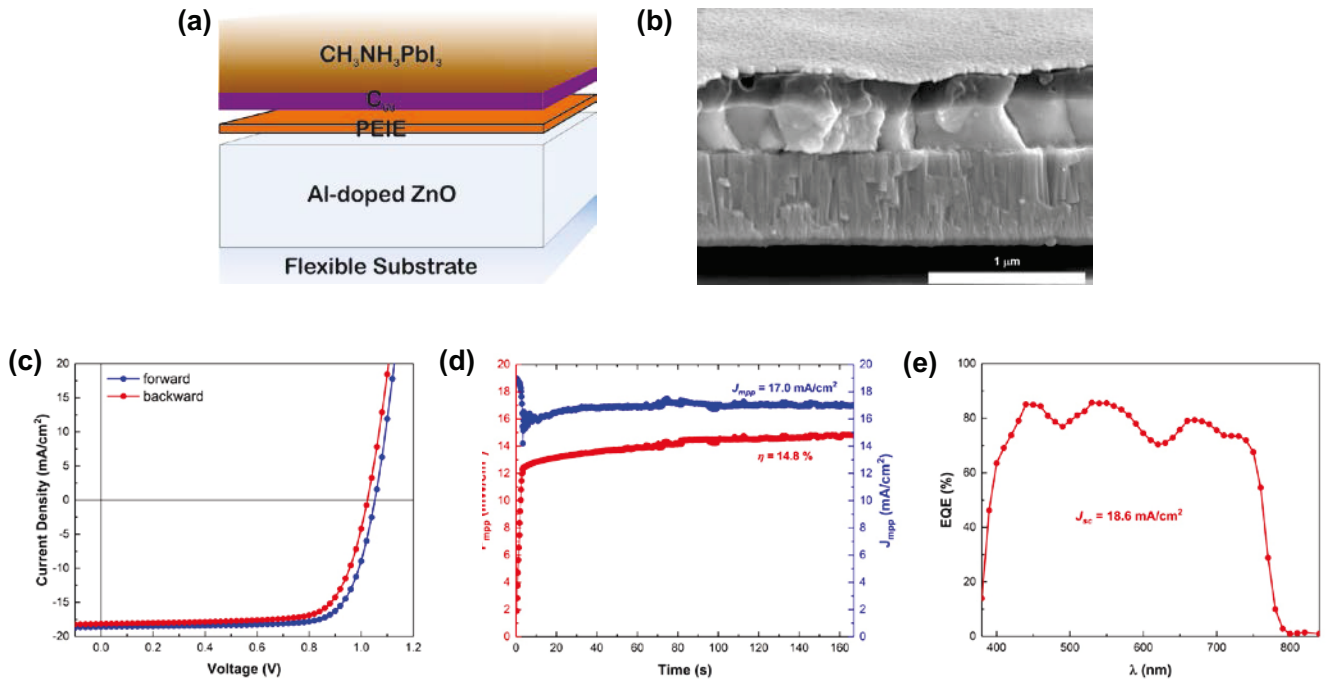


Fig. 3. (a) Schematic of interfacial modification by PEIE deposition. (b) Cross-section SEM image of the flexible PSC (scale bar 1 μm). (c) J - V curves in the forward (blue line), -0.1 V to 1.4 V, and the backward scan (red line), 1.4 V to -0.1 V, measured under standard test conditions. (d) Steady-state output at the MPP of the cell under continuous simulated AM1.5G one sun illumination. Stabilized power output (red line) and J_{MPP} (blue line). (e) EQE spectrum. The calculated J_{sc} from the EQE curve is 18.6 mA cm^{-2} .

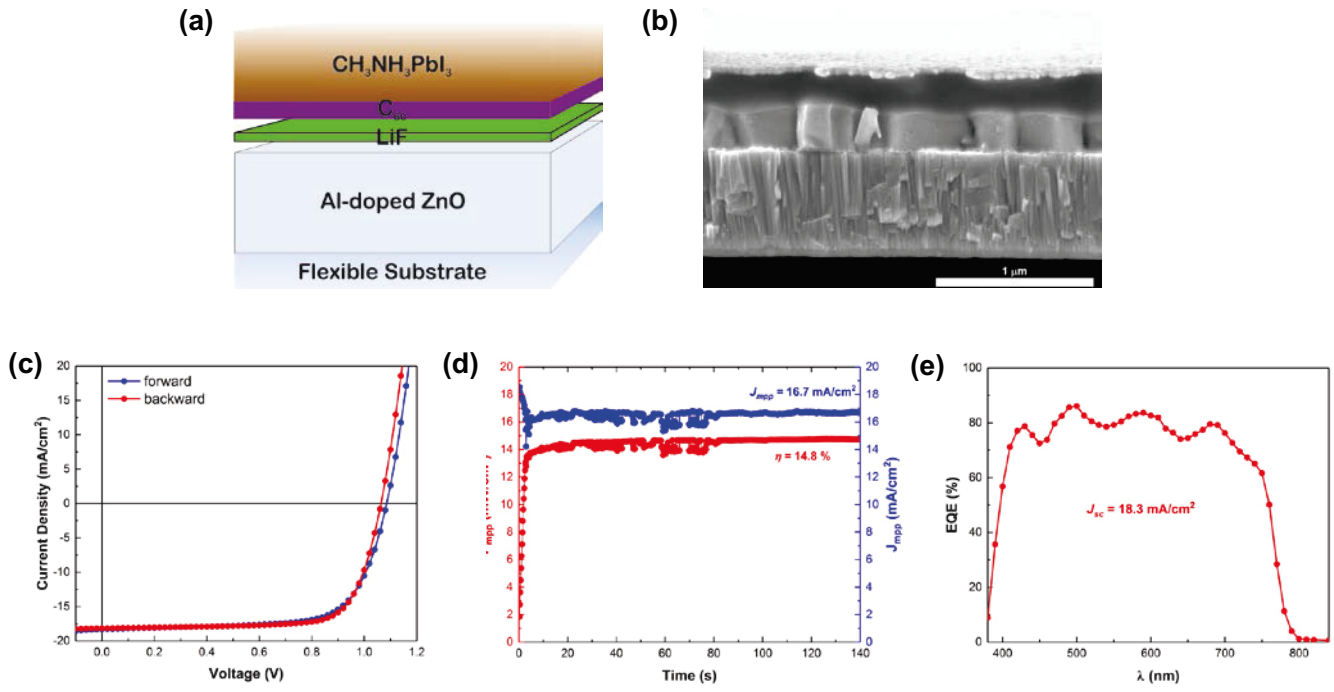


Fig. 4. (a) Schematic of interfacial modification by LiF deposition. (b) Cross-section SEM image of the flexible PSC (scale bar $1\ \mu\text{m}$). (c) J - V curves in the forward (blue line), $-0.1\ \text{V}$ to $1.4\ \text{V}$, and the backward scan (red line), $1.4\ \text{V}$ to $-0.1\ \text{V}$, measured under standard test conditions. (d) Steady-state output at the MPP of the cell under continuous simulated AM1.5G one sun illumination. Stabilized power output (red line) and J_{MPP} (blue line). (e) EQE spectrum. The calculated J_{sc} from the EQE curve is $18.3\ \text{mA cm}^{-2}$.

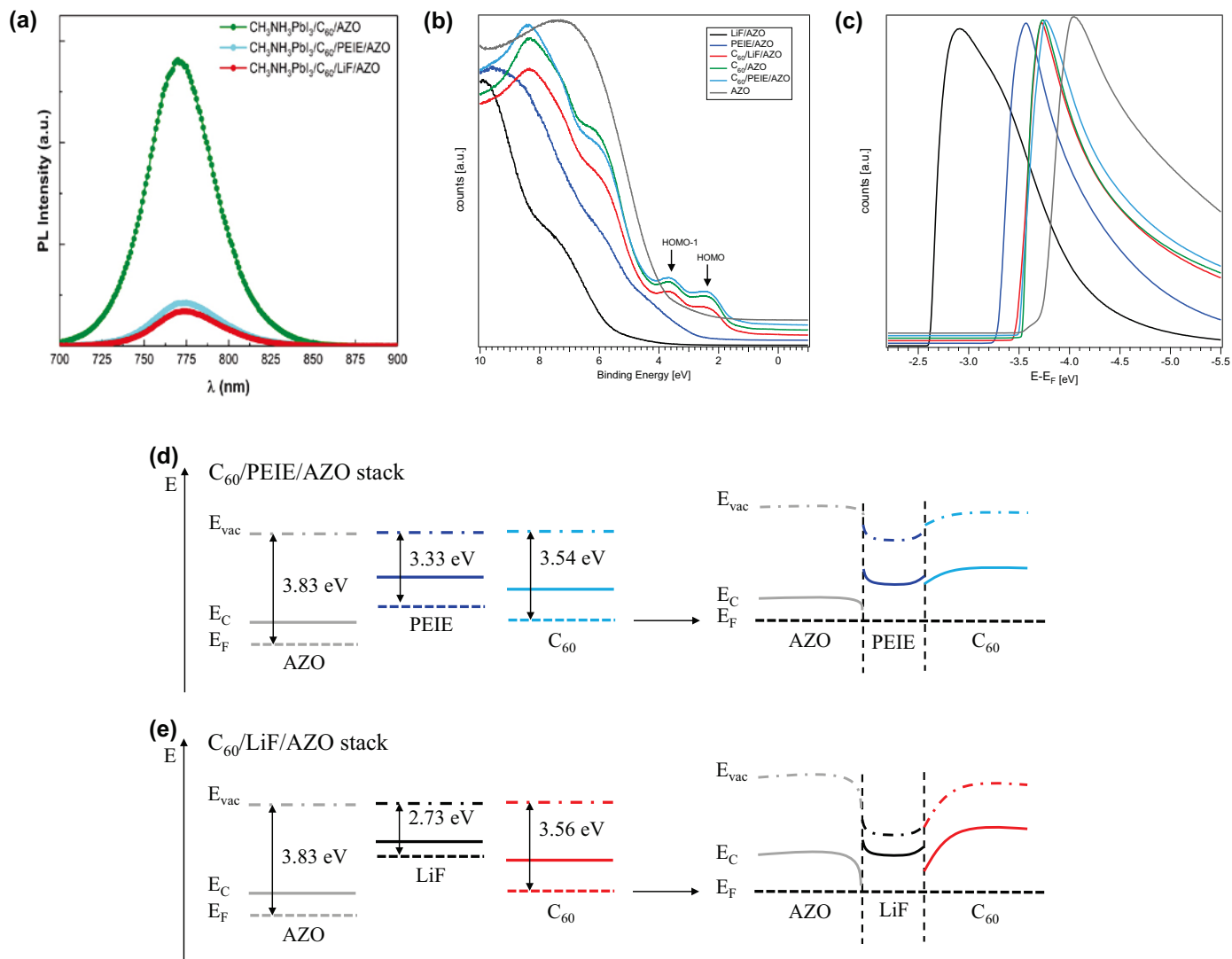


Fig. 5. (a) Comparison between steady-state PL spectra of $\text{CH}_3\text{NH}_3\text{PbI}_3$ films on C_{60}/AZO , $\text{C}_{60}/\text{PEIE}/\text{AZO}$ and $\text{C}_{60}/\text{LiF}/\text{AZO}$ flexible substrates. (b) He I (21.2 eV) UPS spectra of the valence states for AZO, C_{60}/AZO , PEIE/AZO, LiF/AZO, $\text{C}_{60}/\text{PEIE}/\text{AZO}$ and $\text{C}_{60}/\text{LiF}/\text{AZO}$ flexible substrates. (c) Secondary electron cut-off region of the UPS spectra shown in (b) (the spectra are vertically offset for better visibility). (d) Schematics of electrostatic potential modulation with PEIE interfacial modification. (e) Schematics of electrostatic potential modulation with LiF interfacial modification.

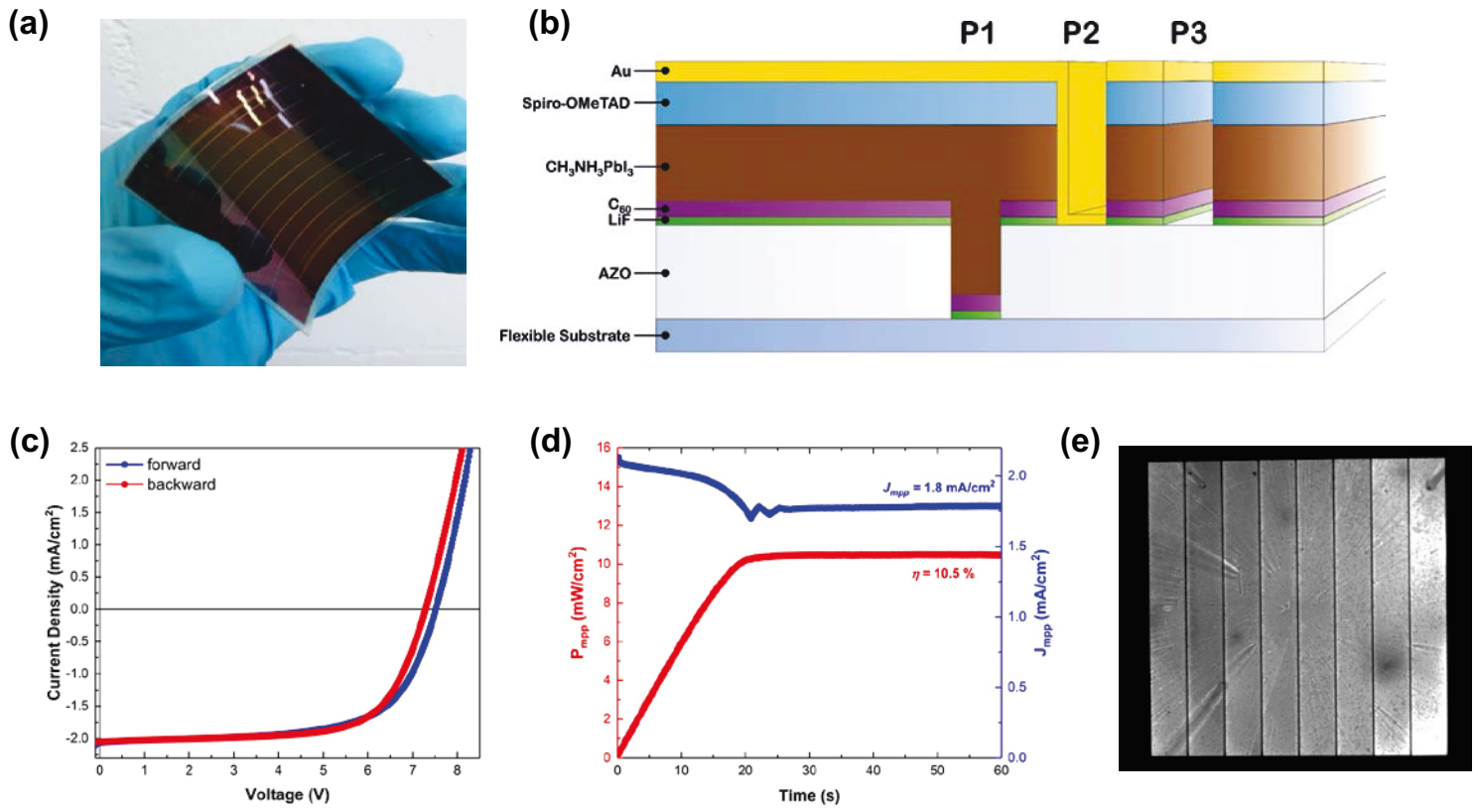


Fig. 6. (a) Photograph of flexible perovskite mini-module. (b) Schematic of monolithically integrated mini-module using three scribing steps P1, P2 and P3. (c) J - V curves in the forward (blue line), -0.1 V to 1.4 V, and the backward scan (red line), 1.4 V to -0.1 V, measured under standard test conditions. (d) Steady-state output at the MPP of the cell under continuous simulated AM1.5G one sun illumination. Stabilized power output (red line) and J_{MPP} (blue line). (e) Electroluminescence imaging of the flexible perovskite mini-module.

References

- [1] W.S. Yang, B.W. Park, E.H. Jung, N.J. Jeon, Y.C. Kim, D.U. Lee, S.S. Shin, J. Seo, E.K. Kim, J.H. Noh, S.I. Seok, *Science*, 356 (2017) 1376-1379.
- [2] G.C. Xing, N. Mathews, S.Y. Sun, S.S. Lim, Y.M. Lam, M. Gratzel, S. Mhaisalkar, T.C. Sum, *Science*, 342 (2013) 344-347.
- [3] M.A. Green, A. Ho-Baillie, H.J. Snaith, *Nat Photonics*, 8 (2014) 506-514.
- [4] M. Saliba, T. Matsui, K. Domanski, J.Y. Seo, A. Ummadisingu, S.M. Zakeeruddin, J.P. Correa-Baena, W.R. Tress, A. Abate, A. Hagfeldt, M. Gratzel, *Science*, 354 (2016) 206-209.
- [5] H. Yoon, S.M. Kang, J.K. Lee, M. Choi, *Energ Environ Sci*, 9 (2016) 2262-2266.
- [6] D. Yang, R.X. Yang, X.D. Ren, X.J. Zhu, Z. Yang, C. Li, S.Z. Liu, *Advanced Materials*, 28 (2016) 5206-5213.
- [7] C. Bi, B. Chen, H.T. Wei, S. DeLuca, J.S. Huang, *Advanced Materials*, 29 (2017).
- [8] S. Pisoni, F. Fu, T. Feurer, M. Makha, B. Bissig, S. Nishiwaki, A.N. Tiwari, S. Buecheler, *J Mater Chem A*, 5 (2017) 13639-13647.
- [9] C. Roldan-Carmona, O. Malinkiewicz, A. Soriano, G.M. Espallargas, A. Garcia, P. Reinecke, T. Kroyer, M.I. Dar, M.K. Nazeeruddin, H.J. Bolink, *Energ Environ Sci*, 7 (2014) 994-997.
- [10] J.L. Yang, B.D. Siempelkamp, E. Mosconi, F. De Angelis, T.L. Kelly, *Chem Mater*, 27 (2015) 4229-4236.
- [11] S. Nishiwaki, A. Burn, S. Buecheler, M. Mural, S. Pilz, V. Romano, R. Witte, L. Krainer, G.J. Spuhler, A.N. Tiwari, *Prog Photovoltaics*, 23 (2015) 1908-1915.
- [12] F. Di Giacomo, V. Zardetto, A. D'Epifanio, S. Pescetelli, F. Matteocci, S. Razza, A. Di Carlo, S. Licoccia, W.M.M. Kessels, M. Creatore, T.M. Brown, *Adv Energy Mater*, 5 (2015).
- [13] J.S. Yeo, C.H. Lee, D. Jang, S. Lee, S.M. Jo, H.I. Joh, D.Y. Kim, *Nano Energy*, 30 (2016) 667-676.
- [14] J. Dagar, S. Castro-Hermosa, M. Gasbarri, A.L. Palma, L. Cina, F. Matteocci, E. Calabrò, A. Di Carlo, T.M. Brown, *Nano Res*, (2017).
- [15] M.H. Li, Y.H. Huan, X.Q. Yan, Z. Kang, Y. Guo, Y. Li, X.Q. Liao, R.X. Zhang, Y. Zhang, *Chemsuschem*, 11 (2018) 171-177.
- [16] A.N. Cho, N.G. Park, *Chemsuschem*, 10 (2017) 3687-3704.
- [17] H.F. Yang, J.C. Zhang, C.F. Zhang, J.J. Chang, Z.H. Lin, D.Z. Chen, X. Sun, H. Xi, G.Q. Han, Y. Hao, *Sol Energy*, 139 (2016) 190-198.
- [18] H. Zhang, H. Azimi, Y. Hou, T. Ameri, T. Przybilla, E. Spiecker, M. Kraft, U. Scherf, C.J. Brabec, *Chem Mater*, 26 (2014) 5190-5193.
- [19] J. Seo, S. Park, Y.C. Kim, N.J. Jeon, J.H. Noh, S.C. Yoon, S.I. Sang, *Energ Environ Sci*, 7 (2014) 2642-2646.
- [20] A. Cuevas, *Proceedings of the 4th International Conference on Crystalline Silicon Photovoltaics (Siliconpv 2014)*, 55 (2014) 53-62.
- [21] K.A. Bush, A.F. Palmstrom, Z.S.J. Yu, M. Boccard, R. Cheacharoen, J.P. Mailoa, D.P. McMeekin, R.L.Z. Hoyer, C.D. Bailie, T. Leijtens, I.M. Peters, M.C. Minichetti, N. Rolston, R. Prasanna, S. Sofia, D. Harwood, W. Ma, F. Moghadam, H.J. Snaith, T. Buonassisi, Z.C. Holman, S.F. Bent, M.D. McGehee, *Nature Energy*, 2 (2017).
- [22] M. Despeisse, G. Bugnon, A. Feltrin, M. Stueckelberger, P. Cuony, F. Meillaud, A. Billet, C. Ballif, *Appl Phys Lett*, 96 (2010).
- [23] C. Ton-That, A.G. Shard, S. Egger, V.R. Dhanak, M.E. Welland, *Phys Rev B*, 67 (2003).

- [24] A. Walter, S.J. Moon, B.A. Kamino, L. Löfgren, D. Sacchetto, F. Matteocci, B. Taheri, J. Bailat, A.D. Carlo, C. Ballif, S. Nicolay, *Ieee J Photovolt*, 8 (2018) 151-155.
- [25] A.L. Palma, F. Matteocci, A. Agresti, S. Pescetelli, E. Calabro, L. Vesce, S. Christiansen, M. Schmidt, A. Di Carlo, *Ieee J Photovolt*, 7 (2017) 1674-1680.